Influence of Magnetic Eccentricity in Bearingless PM Synchronous Machines

Daniel Dietz and Andreas Binder

Institute for Electrical Energy Conversion, Technical University of Darmstadt, Germany
ddietz@ew.tu-darmstadt.de

Abstract

Bearingless permanent magnet (PM) synchronous machines, used as high-speed drives, typically employ a simple rotor structure. Machines of smaller size are equipped with a solid shaft on which a permanent magnet ring is mounted, protected by a carbon-fiber sleeve. Larger machines often require an additional rotor sheet package and use permanent magnet shells instead of a ring.
Since the permanent magnet exhibits a small yield strength, no shrink-fitting between the magnet ring and the shaft can be applied. Thus, the PM ring is required to be slightly bigger in inner diameter than the shaft in outer diameter, leading to a half-moon shaped air gap between magnet and shaft. Although this air gap is usually in the μm-range it can lead to a considerable rotational-frequent radial disturbing force. We discuss the influences, such as the rotor diameter and the pole count, which contribute to this magnetic eccentricity problem. We also show the disturbing influence on the rotor position control by measurements on a built prototype.

1 Introduction

Bearingless Motors (BM) have gained rising attractiveness in the past decade [3]. The most promising topology for industrial high-speed applications such as pumps or compressors is the bearingless permanent magnet (PM) synchronous machine. Several prototypes of this topology have reached high speed values up to 100 000 min^{-1} [4] and 60 kW [5].
One of the key properties that makes PM machines suitable for high-speed operation is the simple composition of the rotor. Typically, it is composed of a massive magnetic steel shaft on which a solid PM ring of low pole count is glued. For bigger diameters, often PM shells are used. The permanent magnet is retained by a protecting carbon- or glas-fiber bandage (Fig. 1c). The bandage is mounted onto the PM by shrink-fitting. Such a shrink-fitting is possible, since the PM exhibits a very high compressive ultimate strength (Table 1). The chosen undersize

Table 1: PM material properties, used for the prototype machine [1, 2]

	Sm_2Co_{17}	NdFeB
Remanence flux density (100 °C) B_{rem} / T	0.96	1.13
Relative permeability $\mu_{\mathrm{r,PM}}$	1.056	1.068
Compressive ultimate strength $R_{\mathrm{m,comp}}$ / $\mathrm{N \cdot mm^{-2}}$	650	925
Tensile ultimate strength R_{m} / $\mathrm{N \cdot mm^{-2}}$	95	90
Density ρ / $\mathrm{kg \cdot m^{-3}}$	8300	7650
Undesired eccentricity air gap δ_{ecc} / μm	50	180

Table 2: Dimensions of the prototype machine

Axial active length l_{Fe} / mm	40
Stator outer / inner radius $r_{\mathrm{s,o}}$/ $r_{\mathrm{s,i}}$ / mm	37.5 / 17.5
Shaft radius r_{sh} / mm	12.25
PM height h_{PM} / mm	2.75
Bandage height + mechanical air gap width: δ / mm	2.5

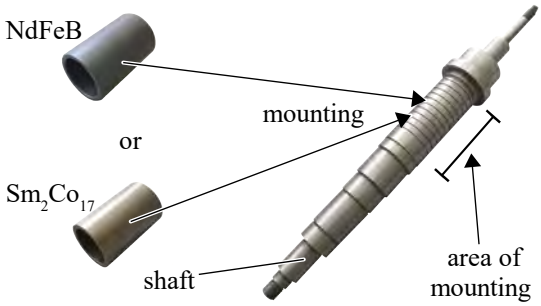

(a) Rotor components

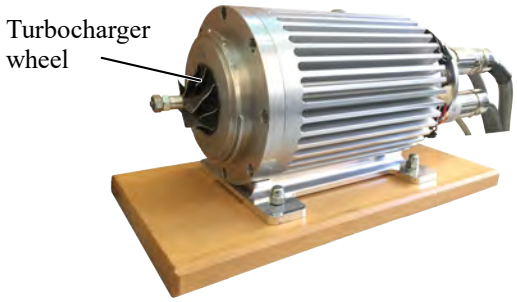

(b) Assembled motor

(c) Wound stator

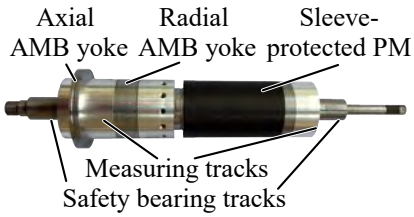

(d) Assembled rotor

Figure 1: Built 1 kW / 60000 min^{-1} bearingless PM synchronous machine and simplified 2D finite element model

between bandage and PM must be chosen to avoid a loss of contact between PM and shaft at high-speed and to stay below the bandage material's yield strength [6]. The choice of this shrink-fitting is by far the most crucial part of the rotor assembly. Thus, little attention is paid to the mounting of the permanent magnet onto the steel shaft. However, this mounting (Fig. 1a) is also problematic, since the PM only exhibits a very low tensile ultimate strength R_{m} (Table 1). Therefore, the PM must be mounted onto the shaft without any undersize, so that a small single-sided air gap δ_{ecc} (Fig. 2) between PM and shaft can occur, which is rotor-fixed. This single-sided air gap leads to a flux concentration at the opposite side of the maximum eccentricity air gap width δ_{ecc} (Fig.2b), resulting in a modulation of the fundamental air gap field (Fig. 2c).
This paper shows that even very small values $\delta_{\mathrm{ecc}} < 200$ μm (here: < 1.6 % of the shaft radius r_{sh}, Table 2) lead to a considerable, disturbing radial force F_{ecc} on the rotor. We discuss, how this magnetic eccentricity influences the operation of bearingless machines. The investigations are carried out for two rotors, one with a Sm_2Co_{17} PM and one with a NdFeB PM, at a built prototype with 1 kW at a speed of $n = 60\,000$ min^{-1}. The two PM rings differ in remanence

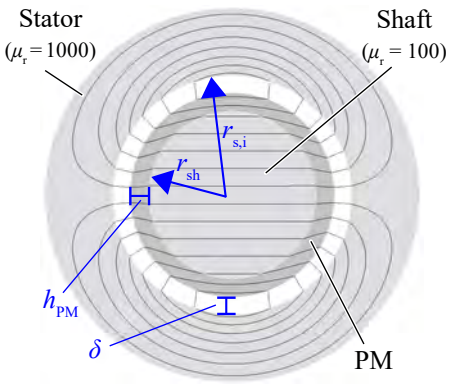

(a) "Healthy" machine: field plot and model geometry

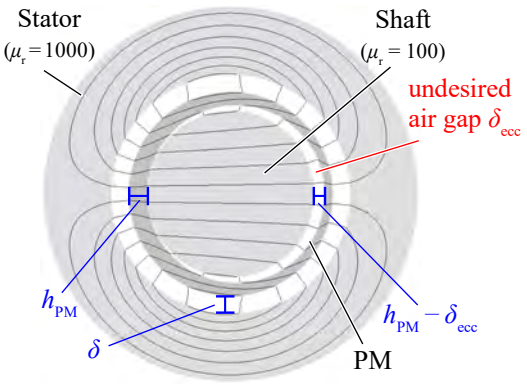

(b) "Unhealthy" machine: field plot and model geometry with undesired air gap δ_{ecc}

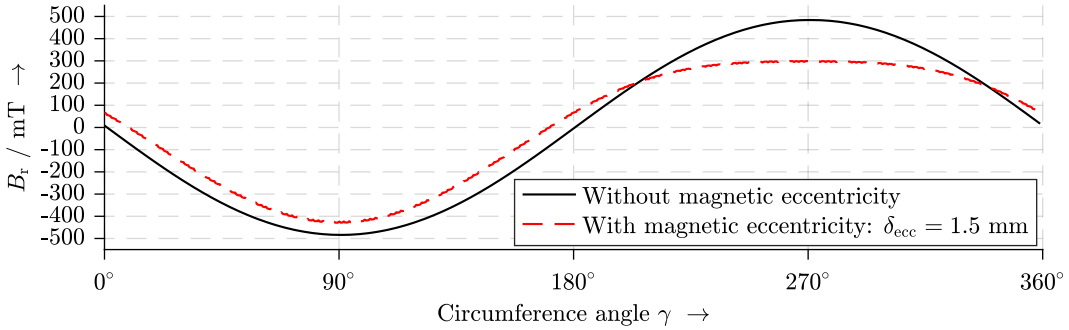

(c) Simulated radial component of the air gap flux density B_r with and without eccentricity

Figure 2: Visualization of the magnetic eccentricity, exemplary with an non-realistically big eccentricity air gap width $\delta_{ecc} = 1.5$ mm

flux density (Table 1). They also exhibit a different eccentricity air gaps δ_{ecc} which occurred unintentionally. We additionally show, how the eccentricity force is influenced by the machine's size, pole count and PM height.

2 Forces due to Magnetic Eccentricity

To calculate the forces on the rotor, the *Maxwell* stress tensor (2) is evaluated over a cylindrical surface of length l_{Fe} and radius $r_\delta = r_{s,i} - \delta/2$ (1). l_{Fe} is the machine's axial iron length, $r_{s,i}$ the bore radius and δ the sum of the air gap width and the bandage height (Table 2). The radial and tangential air gap field components B_r and B_γ are given as the sum of the rotor and stator field waves.

$$\begin{pmatrix} F_x(t) \\ F_y(t) \end{pmatrix} = \int_0^{l_{Fe}} \int_0^{2\pi} \begin{pmatrix} f_r(\gamma,t) \cdot \cos(\gamma) - f_\gamma(\gamma,t) \cdot \sin(\gamma) \\ f_r(\gamma,t) \cdot \sin(\gamma) + f_\gamma(\gamma,t) \cdot \cos(\gamma) \end{pmatrix} \cdot \mathrm{d}\gamma \mathrm{d}z \tag{1}$$

$$\begin{pmatrix} f_r(\gamma,t) \\ f_\gamma(\gamma,t) \end{pmatrix} \Bigg|_{r=r_\delta} = \frac{1}{2 \cdot \mu_0} \cdot \begin{pmatrix} B_r^2(r_\delta,\gamma,t) - B_\gamma^2(r_\delta,\gamma,t) \\ 2 \cdot B_r(r_\delta,\gamma,t) \cdot B_\gamma(r_\delta,\gamma,t) \end{pmatrix} \tag{2}$$

Usually in high-speed bearingless machines the radial component of the rotor air gap field amplitude $\hat{B}_{\mathrm{R},p,p,\mathrm{r}}$ with pole count $2p$ is much bigger than the stator field. In the considered bearingless machine prototype the rotor air gap field is about 15 times higher than the stator field. Therefore, it is neglected in the analysis. Eccentricity problems can be analytically calculated by using the so-called bi-linear conformal mapping method [7]. Alternatively, the perturbation method according to [8, 9] can be used. Here, a magnetostatic 2-dimensional finite element method simulation with magnetically linear and isotropic material assumption is used instead, based on the *JMAG Designer 19.1*. In this section, only the occurrence of the eccentricity-originated additional air gap field waves $B_{\mathrm{ecc},\mu,k,\mathrm{r}}$ is explained qualitatively, which lead to the eccentricity force F_{ecc}.
The radial (subscript: r) rotor (subscript: R) flux density wave $B_{\mathrm{R},\mu,k,\mathrm{r}}(r_\delta,\gamma,t)$ in the air gap of a PM machine at $r = r_\delta$ is approximately given by (3) if a 1-dimensional air gap field is assumed. γ is the mechanical circumference angle in stator-fixed-coordinates, k is the time harmonic order, which is always $k = p$ for the fundamental field wave in stator-fixed coordinates. μ is the absolute space harmonic order, which is always $\mu = p$ for the fundamental field wave. c is the ratio of the PM height h_{PM} to the air gap width δ.

$$B_{\mathrm{R},\mu,k,\mathrm{r}}(r_\delta,\gamma,t) = -\frac{h_{\mathrm{PM}}}{\delta}\cdot B_{\mathrm{PM},\mu,k,\mathrm{r}}(r_\delta,\gamma,t) = c(\gamma,t)\cdot B_{\mathrm{PM},\mu,k,\mathrm{r}}(r_\delta,\gamma,t) \tag{3}$$

The single-sided air gap δ_{ecc} (Fig. 2) leads to a PM height $h_{\mathrm{PM}}(\gamma,t)$ and air gap width $\delta(\gamma,t)$, which vary with the circumference angle γ and time t in stator-fixed coordinates (4), (5). Thus, the radio $c(\gamma,t)$ also varies (6), which can be approximated by (7).

$$h_{\mathrm{PM}}(\gamma,t) \approx h_{\mathrm{PM}} - \frac{\delta_{\mathrm{ecc}}}{2} + \frac{\delta_{\mathrm{ecc}}}{2}\cdot\cos(\gamma - 2\pi\cdot n\cdot t + \varphi_{\mathrm{ecc}}) \tag{4}$$

$$\delta(\gamma,t) \approx \delta + \frac{\delta_{\mathrm{ecc}}}{2} - \frac{\delta_{\mathrm{ecc}}}{2}\cdot\cos(\gamma - 2\pi\cdot n\cdot t + \varphi_{\mathrm{ecc}}) \tag{5}$$

$$c(\gamma,t) = -\frac{h_{\mathrm{PM}}(\gamma,t)}{\delta(\gamma,t)} = c_0 + \sum_{i=1}^{\infty}\hat{c}_i\cdot\cos(i\cdot\gamma - i\cdot 2\pi\cdot n\cdot t + \varphi_{\mathrm{ecc}}) \tag{6}$$

$$\approx \underbrace{-\frac{h_{\mathrm{PM}} - \frac{\delta_{\mathrm{ecc}}}{2}}{\delta + \frac{\delta_{\mathrm{ecc}}}{2}}}_{c_0} + \hat{c}_1\cdot\cos(\gamma - 2\pi\cdot n\cdot t + \varphi_{\mathrm{ecc}}) \tag{7}$$

By inserting (7) into (3), the PM magnetization wave is modulated by its shape via the ratio $c(\gamma,t)$. With the used simplification, the modulation leads to the rotor air gap radial field fundamental (8) in stator-fixed coordinates. Additionally, the air gap fields waves $B_{\mathrm{ecc},\mu,k,\mathrm{r}}$ occur (9). Owing to the model deficiency, (9) for 2-pole rotors also results in a zero$^{\mathrm{th}}$ order space harmonic, which does not exist in reality.

$$B_{\mathrm{R},\mu=p,k=p,\mathrm{r}}(r_\delta,\gamma,t) = \underbrace{c_0\cdot\hat{B}_{\mathrm{PM},p,p,\mathrm{r}}}_{\hat{B}_{\mathrm{R},p,p,\mathrm{r}}(r_\delta)}\cdot\cos(p\cdot\gamma - 2\pi\cdot n\cdot p\cdot t + \varphi_{\mathrm{R}}) \tag{8}$$

$$B_{\mathrm{ecc},\mu,k,\mathrm{r}}(r_\delta,\gamma,t) = \frac{\hat{B}_{\mathrm{PM},p,p,\mathrm{r}}\cdot\hat{c}_1}{2}\cdot\cos\left[\underbrace{(p\pm 1)}_{\substack{\text{spatial}\\ \text{order }\mu}}\cdot\gamma - \underbrace{(p\pm 1)}_{\substack{\text{time}\\ \text{order }k}}\cdot 2\pi\cdot nt + \varphi_{\mathrm{R}} \pm \varphi_{\mathrm{ecc}}\right] \tag{9}$$

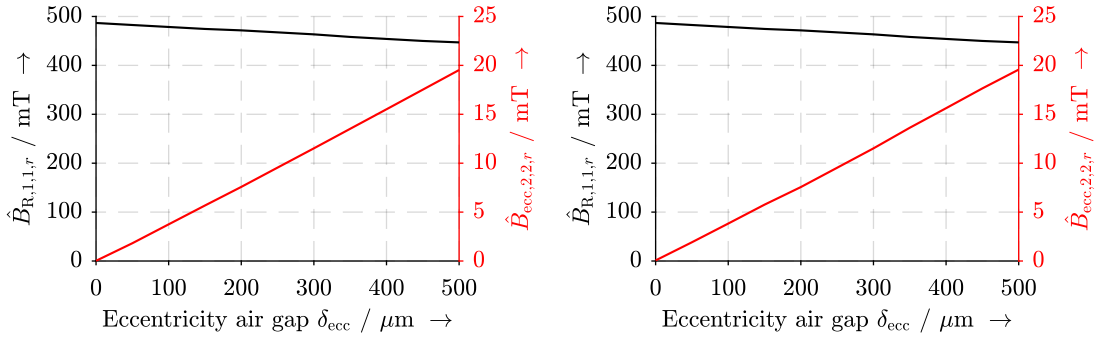

(a) Eccentricity air gap under pole: $\varphi_{\mathrm{ecc}} = 0$ (b) Eccentricity air gap under pole gap: $\varphi_{\mathrm{ecc}} = \frac{\pi}{2}$

Figure 3: Simulated radial magnetic field waves due to the eccentricity air gap δ_{ecc} for a 2-pole rotor with dimensions according to Figure 1c (magnetically linear material assumption according to Table 2 and $B_{\mathrm{rem}} = 1$ T)

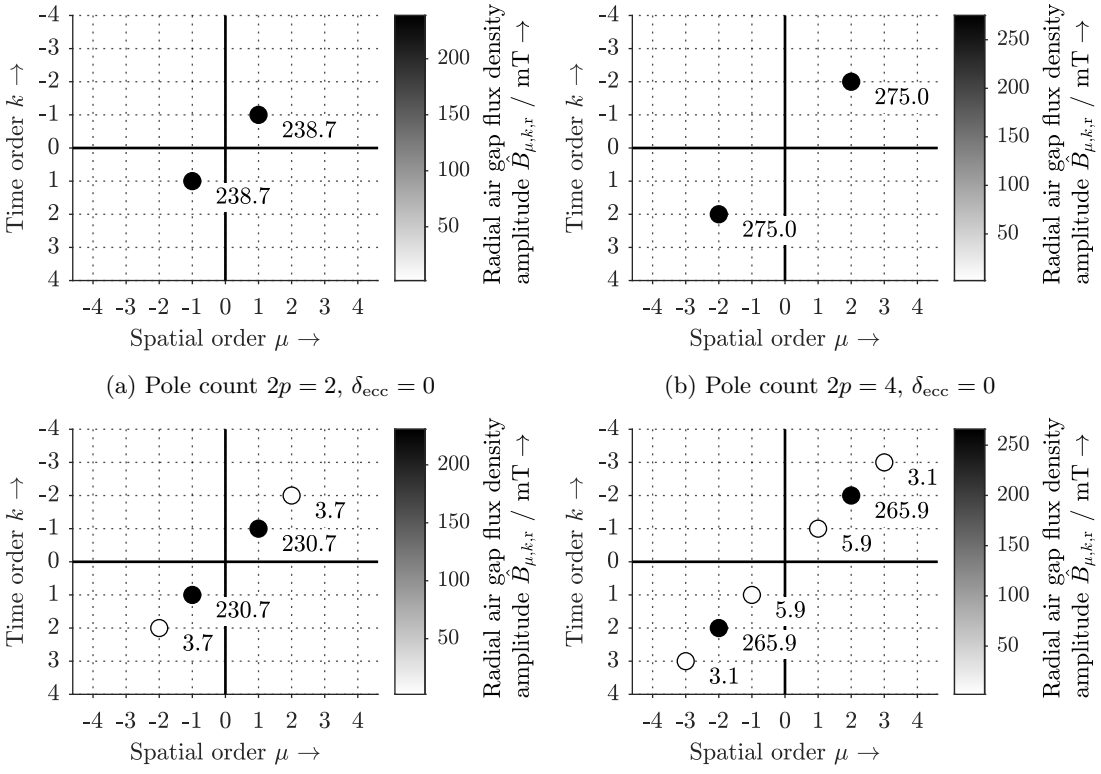

(a) Pole count $2p = 2$, $\delta_{\mathrm{ecc}} = 0$ (b) Pole count $2p = 4$, $\delta_{\mathrm{ecc}} = 0$

(c) Pole count $2p = 2$, $\delta_{\mathrm{ecc}} = 100$ μm (d) Pole count $2p = 4$, $\delta_{\mathrm{ecc}} = 100$ μm

Figure 4: 2D *Fourier* spectrum of the air gap flux density radial component $\hat{B}_{\mathrm{r}}$ in stator reference frame from 2D finite element simulation (k: time harmonic order μ: space harmonic order, evaluated at radius $r_{\mathrm{s,i}} - \delta/2$)

In the considered prototype machine with $2p = 2$ poles, the eccentricity air gap δ_{ecc} leads to a radial field wave $B_{\mathrm{ecc},2,2,\mathrm{r}}$ of time order $k = 2$ and space order $\mu = 2$. Under magnetically linear material assumptions, the amplitude $\hat{B}_{\mathrm{ecc},2,2,\mathrm{r}}$ of this field wave rises linearly with the width of the eccentricity air gap δ_{ecc} (Fig. 3). Note that $\hat{B}_{\mathrm{ecc},2,2,\mathrm{r}}$ does not depend on the location of the eccentricity air gap (angle φ_{ecc}), so that the values in Fig. 3a are equal to Fig. 3b. Thus, in the following analysis we set $\varphi_{\mathrm{ecc}} = 0$, so that the eccentricity air gap is located under the pole.
The amplitude of the fundamental rotor field wave $\hat{B}_{\mathrm{R},1,1,\mathrm{r}}$ decreases linearly in Fig. 3 according to c_0 (7). The rated suspension winding air gap field amplitude is $\hat{B}_{\mathrm{L},2,1,\mathrm{r}} = 8$ mT for the prototype machine. Since the modulated air gap field wave takes values $B_{\mathrm{ecc},2,2,\mathrm{r}} > 5$ mT for $\delta_{\mathrm{ecc}} > 130$ μm (Fig. 3), even small eccentricity values can lead to radial force amplitudes in the range of the rotor gravitational force. Compared to the rotor field fundamental, the modulated field waves due to eccentricity are approximately smaller by factor 50. Thus, they may cause crucial rotor forces but they certainly will not cause considerable additional iron losses. So, a loss analysis of the eccentricity effect is omitted.
A more general representation of the air gap field wave harmonics is given in Fig. 4, which shows the 2-dimensional *Fourier* spectrum of the air gap field radial component B_{r}, used in (2), with respect to time order k and space order μ [10]. Fig. 4b and 4d give the results for the 4-pole rotor with the same motor dimensions (Table 2). Fig. 4a and Fig. 4c show the 2-pole rotor results. Fig. 4c and Fig. 4d show that – due to the eccentricity – additional field waves $B_{\mathrm{ecc},\mu,k,\mathrm{r}}$ occur with the time and space harmonic orders according to (9). The integration of the *Maxwell* stress tensor (1) is zero for all combinations of two field waves with space orders μ_1, μ_2 for which $\mu_1 \neq \mu_2 \pm 1$ holds. For $\mu_1 = \mu_2 \pm 1$ the radial eccentricity force F_{ecc} on the rotor into an arbitrary direction, e.g. in x-direction ($F_{\mathrm{x,ecc}} = F_{\mathrm{ecc}}$), is given in (10) for k_1 and k_2 being the time harmonic orders of the involved field waves. The tangential field components are neglected here for simplicity. For 2-pole machines, F_{ecc} is given in (11), for 4-pole machines the eccentricity force is composed of (12), (13).

$$F_{\mathrm{ecc}}(t) = \frac{\pi \cdot r_\delta \cdot l_{\mathrm{Fe}}}{2 \cdot \mu_0} \cdot B_{\mu_1,k_1,\mathrm{r}}(r_\delta) \cdot B_{\mu_2,k_2,\mathrm{r}}(r_\delta) \cdot \sin((k_2 - k_1)\, 2\pi n t + \varphi_1 \pm \varphi_2) \tag{10}$$

$$F_{\mathrm{ecc}}(t)\,|_{2p=2} = \frac{\pi \cdot r_\delta \cdot l_{\mathrm{Fe}}}{2 \cdot \mu_0} \cdot B_{\mathrm{R},1,1,\mathrm{r}}(r_\delta) \cdot B_{\mathrm{ecc},2,2,\mathrm{r}}(r_\delta) \cdot \sin(2\pi n t + \varphi_{\mathrm{R}} - \varphi_{\mathrm{ecc}}) \tag{11}$$

$$F_{\mathrm{ecc},-}(t)\,|_{2p=4} = \frac{\pi \cdot r_\delta \cdot l_{\mathrm{Fe}}}{2 \cdot \mu_0} \cdot B_{\mathrm{R},2,2,\mathrm{r}}(r_\delta) \cdot B_{\mathrm{ecc},1,1,\mathrm{r}}(r_\delta) \cdot \sin(2\pi n t + \varphi_{\mathrm{R}} + \varphi_{\mathrm{ecc}}) \tag{12}$$

$$F_{\mathrm{ecc},+}(t)\,|_{2p=4} = \frac{\pi \cdot r_\delta \cdot l_{\mathrm{Fe}}}{2 \cdot \mu_0} \cdot B_{\mathrm{R},2,2,\mathrm{r}}(r_\delta) \cdot B_{\mathrm{ecc},3,3,\mathrm{r}}(r_\delta) \cdot \sin(2\pi n t + \varphi_{\mathrm{R}} - \varphi_{\mathrm{ecc}}) \tag{13}$$

This shows that, that the eccentricity air gap δ_{ecc} always leads to a rotational frequent radial force F_{ecc} which depends on the fundamental rotor field wave amplitude $\hat{B}_{\mathrm{R},p,p,r}$ and on the bore radius $r_{\mathrm{s,i}} = r_\delta + \delta/2$. Also F_{ecc} is much higher for 4-pole machines, since two field wave combinations ($\mu_{\mathrm{R}} = 2/\mu_{\mathrm{ecc},1} = 1$ ($\rightarrow F_{\mathrm{ecc},-}$), $\mu_{\mathrm{R}} = 2/\mu_{\mathrm{ecc},2} = 3$ ($\rightarrow F_{\mathrm{ecc},+}$)) contribute to the force generation (Fig. 4d).
The additionally occurring field waves $B_{\mathrm{ecc},\mu,k}$ do no generate eddy current losses in the rotor parts, since these field waves move synchronously with the rotor: Transferring the field wave (5) into rotor-fixed coordinates with the circumference angle $\gamma_{\mathrm{R}} = \gamma - 2\pi \cdot n \cdot t$ leads to the time harmonic order k_{R} in rotor coordinates. Independent of the pole count, for both spectra in Fig. 4, it results $k_{\mathrm{R}} = k - \mu = 0$ due to $k = \mu$. Also in the stator the additional eddy current and hysteresis losses of $B_{\mathrm{ecc},\mu,k}$ may be neglected due to the very small field amplitude compared to the rotor field fundamental (Fig. 3).

3 Influencing Parameters on Eccentricity Forces

The prior section has shown that the eccentricity force oscillates with mechanical rotation frequency $f_\mathrm{m} = n$. In this section, we discuss which machine properties influence the amplitude of this eccentricity force $\hat{F}_\mathrm{ecc}$. Note that $\hat{F}_\mathrm{ecc}$ is not influenced by the angular position φ_ecc (7), (8), (9) of the maximum eccentricity air gap. That means, $\hat{F}_\mathrm{ecc}$ is identical for δ_ecc being located under a pole or under the pole gap (Fig. 3).
Fig. 5a (5b) indicates the eccentricity force amplitude $\hat{F}_\mathrm{ecc}$ for a 2-pole (4-pole) rotor topology in dependence of the eccentricity air gap width $\delta_\mathrm{ecc} = 0,\ 50\ \mu\mathrm{m},\ 100\ \mu\mathrm{m},\ ...,\ 500\ \mu\mathrm{m}$ and the PM remanence flux density $B_\mathrm{rem} = 0.8\ \mathrm{T},\ 0.9\ \mathrm{T},\ ...,1.3\ \mathrm{T}$. The remanence flux density has low influence on $\hat{F}_\mathrm{ecc}$ for small values of δ_ecc and for large values of B_rem. The eccentricity force in a 4-pole topology is approximately bigger by factor 3 compared to 2-pole rotors which was explained in Section 2. The values of the two 2-pole rotors, used for the prototype machine, are marked in Fig. 5a. The NdFeB-rotor with the higher B_rem-value is more prone to eccentricity forces than the Sm_2Co_{17}-rotor. The eccentricity air gap is $\delta_\mathrm{ecc} = 50\ \mu\mathrm{m}$ for the Sm_2Co_{17}-rotor and $\delta_\mathrm{ecc} = 100\ \mu\mathrm{m}$ for the NdFeB-rotor. Thus, the simulated eccentricity force is $\hat{F}_\mathrm{ecc} = 0.9$ N for the Sm_2Co_{17}-rotor and $\hat{F}_\mathrm{ecc} = 3.8$ N for the NdFeB-rotor.
Fig. 6a (6b) indicates the eccentricity force amplitude $\hat{F}_\mathrm{ecc}$ for a 2-pole (4-pole) rotor topology in dependence of the eccentricity air gap width $\delta_\mathrm{ecc} = 0,\ 50\ \mu\mathrm{m},\ 100\ \mu\mathrm{m},\ ...,\ 500\ \mu\mathrm{m}$ and thickness $h_\mathrm{PM} = 1\ \mathrm{mm},\ 1.5\ \mathrm{mm},\ ...,\ 5\ \mathrm{mm}$ of the PM ring. For small values of δ_ecc the PM height does hardly influence the eccentricity force. For high values of δ_ecc the eccentricity force is low if the PM height is rather small or rather big. This is because a big PM height increases the air gap flux density but also increases the magnetically effective air gap $\hat{B}_{\mathrm{R},p,p,r} \propto h_\mathrm{PM}/\left(h_\mathrm{PM} + \delta\right)$. This finding is independent of the pole count, but the eccentricity force is much bigger by approximately factor 3 for the 4-pole compared to the 2-pole topology.
Fig. 7a (7b) gives the eccentricity force amplitude $\hat{F}_\mathrm{ecc}$ for a 2-pole (4-pole) rotor topology in dependence of the eccentricity air gap width $\delta_\mathrm{ecc} = 0,\ 50\ \mu\mathrm{m},\ 100\ \mu\mathrm{m},\ ...,\ 500\ \mu\mathrm{m}$ and the stator inner diameter $2 \cdot r_\mathrm{s,i} = 20\ \mathrm{mm},\ 25\ \mathrm{mm},\ ...,\ 100\ \mathrm{mm}$ at $B_\mathrm{rem} = 1$ T. The PM height h_PM

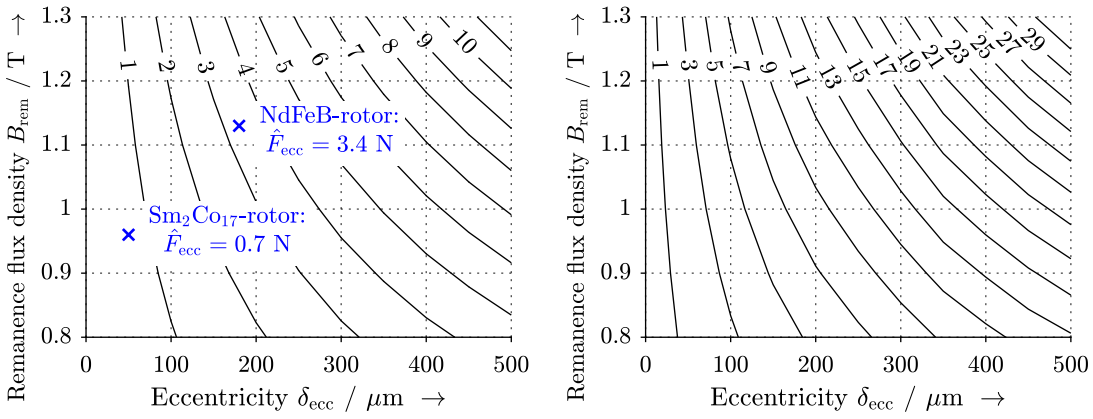

(a) Pole count $2p = 2$ (b) Pole count $2p = 4$

Figure 5: Simulated radial magnetic eccentricity force $\hat{F}_\mathrm{ecc}$ in N for varying magnetic eccentricity air gap width δ_ecc and varying remanence flux density B_rem (dimensions according to Table 2, assumption of magnetically linear materials)

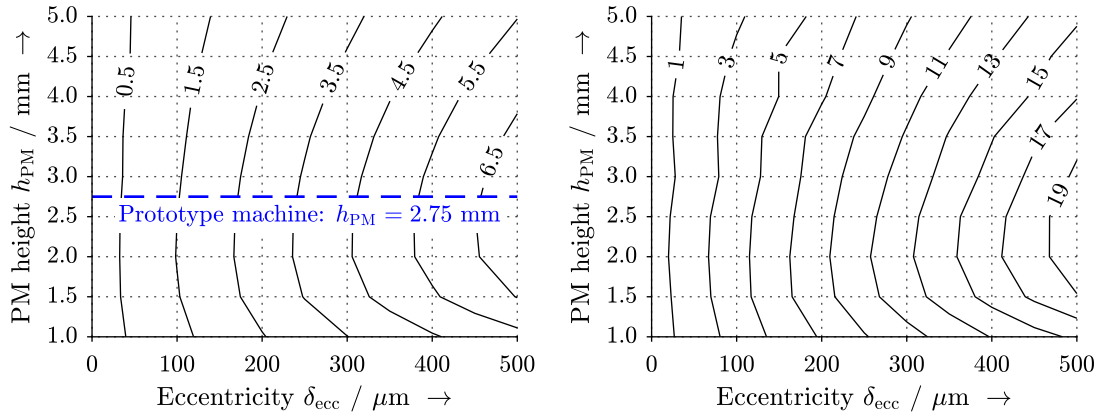

(a) Pole count $2p = 2$ (b) Pole count $2p = 4$

Figure 6: Simulated radial magnetic eccentricity force $\hat{F}_{ecc}$ in N for varying magnetic eccentricity air gap width δ_{ecc} and varying PM height h_{PM} ($B_{rem} = 1$ T,dimensions according to Table 2, assumption of linear materials)

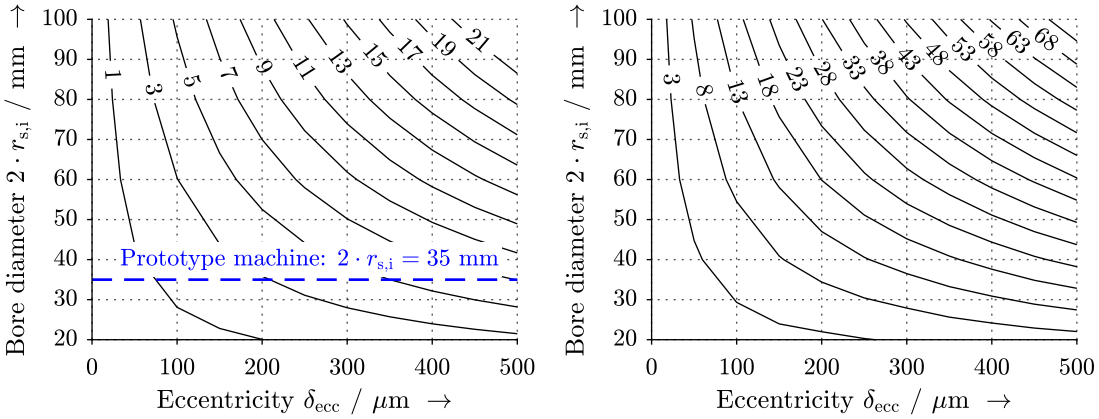

(a) Pole count $2p = 2$ (b) Pole count $2p = 4$

Figure 7: Simulated radial magnetic eccentricity force $\hat{F}_{ecc}$ in N for varying magnetic eccentricity air gap width δ_{ecc} and varying stator bore diameter $2 \cdot r_{s,i}$ ($B_{rem} = 1$ T, $h_{PM} = 2.75$ mm, $\delta + h_b = 2.5$ mm, assumption of linear materials)

and the shaft radius is kept constant ($h_{PM} = 2.75$ mm, $r_{sh} = 12.25$ mm). The bore diameter $2 \cdot r_{s,i}$ and the eccentricity air gap width δ_{ecc} both increase the $\hat{F}_{ecc}$-values to the same extent. In (5) $r_{s,i}$ is included linearly. Also in Fig. 3 the linear relationship between δ_{ecc} and the modulated air gap field wave $\hat{B}_{ecc,\mu,k,r}$ is proved. Therefore, especially machines with large bore diameters are prone to magnetic eccentricity-originated forces. The findings are independent of the pole count, but the eccentricity force is much bigger by approximately factor 3 for the 4-pole compared to the 2-pole topology.

4 Measurements and Influence on Rotor Position Control

At the prototype machine (Fig. 1) the suspension currents for horizontal rotor forces $i_{\mathrm{d,L}}$ and for vertical rotor forces $i_{\mathrm{q,L}}$ were measured at rotor standstill for 10 different equidistant rotor angle positions (Fig. 9). The currents are averaged over 1 s. Since the rotor position is constant, the dynamic controller properties are excluded from the measurements. The rotor is – according to the calibrated radial eddy current position sensors – in the concentric position. It is aligned with the vertical axis to avoid the influence of the gravitational force.
The measurement was conducted with the Sm_2Co_{17}-rotor (Fig. 9a) and with the NdFeB-rotor (Fig. 9b). Both rotors exhibit a sine- and cosine-shaped radial disturbing force, which is compensated by the suspension currents $i_{\mathrm{d,L}}$ and $i_{\mathrm{q,L}}$. Consequently, this radial force wave of amplitude $\hat{F}_{\mathrm{ecc}}$ rotates synchronously with the rotor (time order $k = 1$).
The measured suspension force-current coefficients are $k_{\mathrm{F,Nd}} = 1.09\ \mathrm{N \cdot A^{-1}}$ for the NdFeB-rotor and $k_{\mathrm{F,Sm}} = 1.01\ \mathrm{N \cdot A^{-1}}$ for the Sm_2Co_{17}-rotor. The AC component of the suspension force is $\hat{i}_{\mathrm{ecc}} = 3.42$ A for the NdFeB-rotor and $\hat{i}_{\mathrm{ecc}} = 0.83$ A for the Sm_2Co_{17}-rotor. Thus, the eccentricity forces are determined to be $\hat{F}_{\mathrm{ecc}} = 3.7$ N for the NdFeB-rotor and $\hat{F}_{\mathrm{ecc}} = 0.83$ N for the Sm_2Co_{17}-rotor. These results agree with the simulation results at $\delta_{\mathrm{ecc}} = 180\ \mu$m for the NdFeB-rotor (simulated: $\hat{F}_{\mathrm{ecc}} = 3.4$ N) and at $\delta_{\mathrm{ecc}} = 50\ \mu$m for the Sm_2Co_{17}-rotor (simulated: $\hat{F}_{\mathrm{ecc}} = 0.7$ N). This eccentricity force $F_{\mathrm{ecc}}(t)$ acts on the rotor according to Figure 8, in which the rotor plant is shown without the tilting motions and the gyroscopic effect for simplicity. The damping and oscillation behavior of the plant is determined by the controller settings, which must overcome the negative magnetic stiffness $k_{\mathrm{s,r}}$ (Fig. 8). In contrast to rotor unbalance forces, the amplitude $\hat{F}_{\mathrm{ecc}}$ of the magnetic eccentricity force is speed-independent. Neglecting the controller influence on the rotor movement and considering only the movement originated by $F_{\mathrm{ecc}}(t)$, the actual amplitude $\hat{x}_{\mathrm{ecc}}$ of the movement due to the eccentricity force decreases with rising speed $n = f_{\mathrm{m}}$ according to *Newton*'s law with $\hat{x}_{\mathrm{ecc}} \propto 1/f_{\mathrm{m}}^2$ (14).

$$F_{\mathrm{ecc}}(t) = \hat{F}_{\mathrm{ecc}} \cdot \sin(2\pi \cdot f_{\mathrm{m}} \cdot t) = m \cdot \ddot{x}_{\mathrm{ecc}} \quad \Rightarrow \quad \hat{x}_{\mathrm{ecc}} = \frac{\hat{F}_{\mathrm{ecc}}}{m \cdot (2\pi \cdot f_{\mathrm{m}})^2} \tag{14}$$

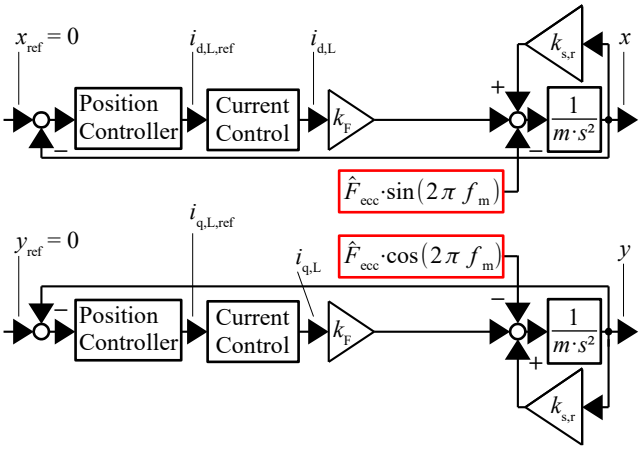

Figure 8: Simplified position controller circuit with eccentricity force F_{ecc}, acting on the rotor plant (neglect of rotor tilting motions and gyroscopic effect)

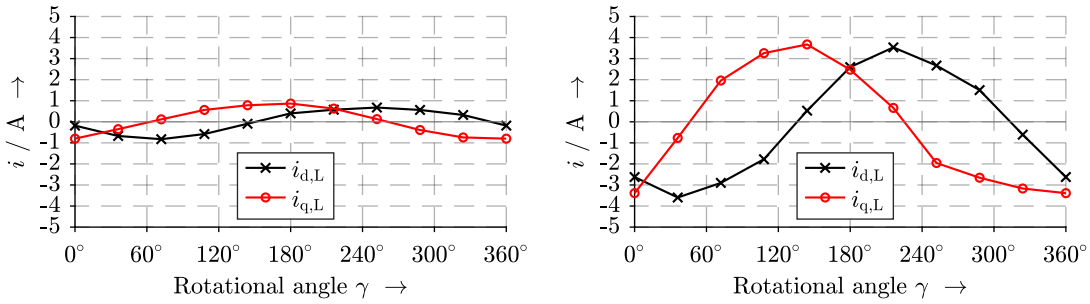

(a) Sm_2Co_{17} (b) NdFeB

Figure 9: Measured currents $i_{d,L}$, related to a bearing force in x-direction, and $i_{q,L}$, related to a bearing force in y-direction at concentric vertical rotor position for a varying rotation angle γ at rotor standstill ($i_{d,L}$, $i_{q,L}$ expected to be zero for no magnetic eccentricity)

Fig. 10a shows the actual x-position of the NdFeB-rotor during a speed-up from $n = f_m = 0$ to $n = f_m = 240$ Hz. Also the red line indicates the theoretical magnetic eccentricity originated rotor movement amplitude $\hat{x}_{ecc}$ according to (14). The rotor's rigid body eigenfrequencies for the chosen controller stiffness are at $f_{eig,1} = 48$ Hz and $f_{eig,2} = 66$ Hz. These eigenfrequencies do not appear in the position signal with increased oscillation amplitudes due to the good damping behavior of the position controller. The rotor orbit decreases from $\hat{x} = 52$ μm at $f_m = 5$ Hz to $\hat{x} = 26$ μm at $f_m = 150$ Hz. This decrease is owing to mechanical "damping" property described in (14). For $f_m > 155$ Hz a "force-free" rotation [11, 12] is enabled by notching out f_m in the position controller feedback signal. By this, the rotor orbit is even decreased due to the poor position controller's disturbance reaction in case of high-frequent disturbances.
Fig. 10b shows the suspension current $i_{d,L}$ for the NdFeB-rotor during a speed-up from $n = f_m = 0$ to $n = f_m = 240$ Hz. The current takes high values up to $\hat{i}_{d,L} = 3$ A at standstill due to magnetic eccentricity forces (Fig. 9b). The current amplitude even increases up to $\hat{i}_{d,L} = 4$ A at $f_m = 150$ Hz, since the position controller's disturbance reaction to the rotational-frequent forces worsens for higher frequencies. Thus, the rotation frequency f_m is notched out of the actual position sensors for $f_m > 155$ Hz. Consequently, the AC component in the suspension current $i_{d,L}$ diminishes.
The effectiveness of the notch filter can also be seen by comparing Fig. 10c (operation at $f_m = 20$ Hz) with Fig. 10d (operation at $f_m = 200$ Hz). At low speed – and, thus, a big eccentricity-originated rotor movement $\hat{x}_{ecc}$ – the position controller counteracts the rotor movement with current nearly in phase opposition to the position signal. At high speed, the rotor orbit is inherently small, since the magnetic eccentricity-originated rotor movement diminishes. Additionally, the position controller shows no reaction to the rotational-frequent rotor oscillation, which occurs due to rotor unbalance.
The investigation shows that the magnetic eccentricity force F_{ecc} does not influence the bearingless machine's operation at speeds $n > 50$ Hz. Even though it is not crucial for high-speed operation, the suspension current amplitudes at low speed can be crucial. This criticality is based on the inverter's current limit. In Fig. 10a, 10b the torque-producing current was only $i_{q,D} = 0.3$ A and, thus, by factor 10 smaller than the suspension current.
For high machine dynamics, the speed-up process may be carried out with high torque-producing current values $i_{q,D}$. Also, the torque producing current leads to radial disturbing force orthogonal to the controller's reference force vector [13], which worsens the controller's

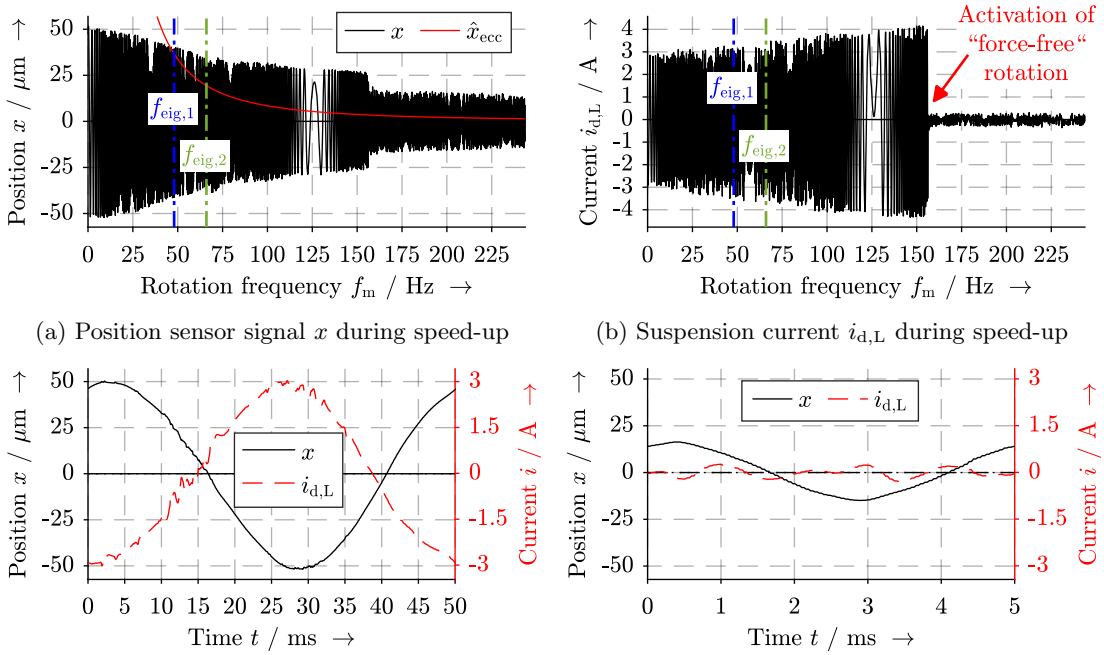

(a) Position sensor signal x during speed-up

(b) Suspension current $i_{\mathrm{d,L}}$ during speed-up

(c) Suspension current $i_{\mathrm{d,L}}$ and position x at rotation with $f = 20$ Hz

(d) Suspension current $i_{\mathrm{d,L}}$ and position x at rotation with $f = 200$ Hz

Figure 10: Measured suspension current and position signal with the NdFeB-rotor at operation with rotation frequency $f < 240$ Hz

reaction to the magnetic eccentricity forces. Therefore, the inverter's current limit may be reached very fast if the magnetic eccentricity force is big and the machine is accelerated fast. For the prototype machine the inverter's current limit is at $i_{\mathrm{max}} = 16$ A (momentary value), which is reached if the torque-producing reference current at zero-speed is $i_{\mathrm{q,D,ref}} > 10$ A. Even though the reference currents are below the inverter's current limit, the over-current protection can trip due to ripple in the actual current, caused by the pulse width modulation. For the considered prototype, values of $i_{\mathrm{q,D,ref}} > 10$ A are only possible at speeds $n = f_{\mathrm{m}} > 150$ Hz.

5 Conclusion

Disturbing radial rotor forces in bearingless PM machines are discussed which have the origin in an undesired half-moon shaped air gap between the permanent magnet and the rotor shaft. The occurring radial force wave rotates with rotor frequency independent of the pole count. Its amplitude increases for PMs with high remanence values and for machines with a large bore diameter. Even for very small eccentricity air gaps of $\delta_{\mathrm{ecc}} < 200$ μm the occurring force amplitude can take considerable values of several N. Measurements on a prototype with a NdFeB-rotor have shown that an eccentricity air gap of $\delta_{\mathrm{ecc}} = 180$ μm leads to high suspension currents, which can reach the inverter's current limit. The resulting rotor orbit is very big at low speed but decreases strongly with speed ($\propto 1/n^2$) due to the rotor mass inertia, since the eccentricity force amplitude is independent of the rotor speed. Thus, at high-speed operation magnetic eccentricity forces are not crucial.

6 Acknowledgments

Funded by the Deutsche Forschungsgemeinschaft (DFG, German Research Foundation) – 437667923, BI 701/22-1 (Gefördert durch die Deutsche Forschungsgemeinschaft (DFG) – 437667923, BI 701/22-1). Supported by KEBA Industrial Automation Germany GmbH.

References

[1] Vacuumschmelze GmbH & Co. KG, "Rare Earth Permanent Magnets Vacodym Vacomax," 2014. [Online]. Available: https://vacuumschmelze.de/shared/quickNav/Downloads

[2] S. Ruoho, M. Haavisto, E. Takala, T. Santa-Nokki, and M. Paju, "Temperature Dependence of Resistivity of Sintered Rare-Earth Permanent-Magnet Materials," *IEEE Transactions on Magnetics*, vol. 46, no. 1, pp. 15–20, Jan. 2010. [Online]. Available: http://ieeexplore.ieee.org/document/5357499/

[3] H.-D. Stölting, E. Kallenbach, and W. Amrhein, Eds., *Handbook of fractional-horsepower drives*. Berlin, Heidelberg, New York: Springer-Verlag, 2008.

[4] Y. Fu, M. Takemoto, S. Ogasawara, and K. Orikawa, "Investigation of Operational Characteristics and Efficiency Enhancement of an Ultra-High-Speed Bearingless Motor at 100,000 r/min," *IEEE Transactions on Industry Applications*, vol. 56, no. 4, pp. 3571–3583, Apr. 2020.

[5] Z. Liu, A. Chiba, Y. Irino, and Y. Nakazawa, "Optimum Pole Number Combination of a Buried Permanent Magnet Bearingless Motor and Test Results at an Output of 60 kW With a Speed of 37000 r/min," *IEEE Open Journal of Industry Applications*, vol. 1, pp. 33–41, Feb. 2020.

[6] A. Borisavljevic, *Limits, Modeling and Design of High-Speed Permanent Magnet Machines*, ser. Springer Theses. Berlin, Heidelberg: Springer-Verlag, 2013.

[7] F. Rezaee-Alam, B. Rezaeealam, and J. Faiz, "Unbalanced Magnetic Force Analysis in Eccentric Surface Permanent-Magnet Motors Using an Improved Conformal Mapping Method," *IEEE Transactions on Energy Conversion*, vol. 32, no. 1, pp. 146–154, 2017.

[8] U. Kim and D. Lieu, "Magnetic field calculation in permanent magnet motors with rotor eccentricity: with slotting effect considered," *IEEE Transactions on Magnetics*, vol. 34, no. 4, pp. 2253–2266, Jul. 1998. [Online]. Available: http://ieeexplore.ieee.org/document/703863/

[9] G. Messager, "Self-bearing permanent magnet synchronous machine configurations and control for high-speed applications," Ph.D. Thesis, Technical University of Darmstadt, Institute for Electrical Energy Conversion, Darmstadt, Germany, Sep. 2019.

[10] N. Erd, R. Koster, and A. Binder, "Computational Analysis of Air Gap Field in Electrical Machines by Fourier Coefficient Matrices," in *2020 International Conference on Electrical Machines (ICEM)*. Gothenburg, Sweden: IEEE, Aug. 2020, pp. 2479–2485. [Online]. Available: https://ieeexplore.ieee.org/document/9270692/

[11] G. Schweitzer and E. H. Maslen, Eds., *Magnetic Bearings: Theory, Design, and Application to Rotating Machinery*. Berlin, Dordrecht, Heidelberg, New York: Springer-Verlag, 2009.

[12] A. Chiba, T. Fukao, O. Ichikawa, M. Oshima, M. Takemoto, and D. Dorrell, *Magnetic bearings and bearingless drives*. Amsterdam, London: Elsevier/Newnes, 2005, oCLC: 179729376.

[13] G. Messager and A. Binder, "Derivation of forces and force interferences in a double conical high-speed bearingless permanent magnet synchronous motor," in *International Electric Machines and Drives Conference (IEMDC)*, Miami, USA, May 2017, pp. 1–8.